A Hydridoaluminate Additive Producing a Protective Coating on Ni-Rich Cathode Materials in Lithium-Ion Batteries

Juan Forero-saboya, Ivan A Moiseev, Marina-lamprini Vlara, Dominique Foix, Michaël Deschamps, Artem M Abakumov, Jean-marie Tarascon, Sathiya Mariyappan

ADVANCED ENERGY MATERIALS
www.advenergymat.de

A Hydridoaluminate Additive Producing a Protective Coating on Ni-Rich Cathode Materials in Lithium-Ion Batteries

*Juan Forero-Saboya, Ivan A. Moiseev, Marina-Lamprini Vlara, Dominique Foix, Michael Deschamps, Artem M. Abakumov, Jean-Marie Tarascon, and Sathiya Mariyappan**

To enhance the energy density of Li-ion batteries, high-capacity and high-voltage cathode materials are needed. Recently, Ni-rich layered oxides have attracted attention as they can offer ≈200 mAh g^{-1} when cycled up to 4.3 V. However, cycling these materials in their full capacity range often leads to excessive reactivity with the electrolyte, resulting in particle cracking, transition metal dissolution, and oxygen loss. In this study, the use of lithium hydridoaluminates as electrolyte additives is explored for lithium-ion batteries based on nickel-rich cathode materials. Being mild reducing agents, these additives act as HF scavengers, avoiding transition metal dissolution from the cathode. Additionally, their oxidation results in the formation of an Al-rich protective layer on the cathode, which dampens the surface reactivity, preventing surface reconstruction and impedance build-up. This study further stresses the important role of the cathode-electrolyte interface phenomena on the capacity degradation of Ni-rich cathode materials and provides a novel avenue for controlling this reactivity, thus extending their cycling life.

1. Introduction

The development of advanced Li-ion batteries requires the use of high-voltage cathode materials, which involves mastering their surface reactivity. Promising cathode materials include the nickel-rich layered oxides with general formula $LiNi_xMn_yCo_{1-x-y}O_2$ (NMC) and $x \geq 0.8$, as they offer high capacity (>200 mAh g^{-1}) within the typical voltage window of 2.0-4.3 V. However, cycling these materials to a near 100% state-of-charge (removing ≈0.7–0.8 Li) causes a severe capacity fade, driven by several interrelated mechano-chemical degradation phenomena.

The commonly held belief attributes the capacity fading to intergranular cracking originating from anisotropic lattice volume changes during cycling, although recent studies suggest that the surface reactivity might be the ultimate culprit.[1] Nickel-rich cathode materials do suffer from an abrupt and non-monotonic change in the unit cell's *c*-axis at high state-of-charge, during the H2→H3 phase transition (Figure S1, Supporting Information), resulting in significant volume contraction. This has been hypothesized to result in particle cracking, pulverization, and increased resistance.[2,3]

J. Forero-Saboya, M.-L. Vlara, J.-M. Tarascon, S. Mariyappan
Chimie du Solide et de l'Energie
UMR 8260
Collège de France
CEDEX 05, Paris 75231, France
E-mail: sathiya.mariyappan@college-de-france.fr

J. Forero-Saboya, M.-L. Vlara, D. Foix, M. Deschamps, J.-M. Tarascon, S. Mariyappan
Réseau sur le Stockage Electrochimique de l'Energie (RS2E)
CNRS FR 3459
Cedex 1, Amiens 80039, France

I. A. Moiseev, A. M. Abakumov
Center for Energy Science and Technology
Skolkovo Institute of Science and Technology
Bolshoy Boulevard 30, bld. 1, Moscow 121205, Russia

M.-L. Vlara, J.-M. Tarascon
Sorbonne Université
4 place Jussieu, Paris 75005, France

D. Foix
Université de Pau et Pays de l'Adour
CNRS
E2S UPPA
IPREM
UMR 5254, Cedex 9, Pau 64053, France

M. Deschamps
CNRS
CEMHTI UPR3079
Université d'Orléans
1D avenue de la recherche scientifique, Cedex 2, Orléans 45071, France

The ORCID identification number(s) for the author(s) of this article can be found under https://doi.org/10.1002/aenm.202402051

DOI: 10.1002/aenm.202402051

However, the surface reactivity might play an even bigger role in the material degradation. At a high state-of-charge (above 4 V), the surface of the cathode oxidizes the electrolyte, promoting oxygen loss and transition metal dissolution (TM) from the material, which result in structural transformations from the initial layered structure to a rock-salt phase. This phase transformation, which initiates at the surface, extends deeper into the active material particles, decreasing the Li^+ cation diffusivity.[4] Additionally, the mismatch between the rock-salt and the layered structures' lattice parameters can be an important cause of internal stress and particle cracking.[5]

It is crucial, thus, to master the surface reactivity of the cathode material particles to ensure a long cycling life. This is traditionally achieved by applying an inert coating layer, such as $LiNbO_3$ or Al_2O_3, which establishes a physical barrier with the electrolyte and provides additional functionalities.[6] However, achieving a thin and fully conformal ex situ coating is challenging and costly. Moreover, having a non-electronic conductor covering the active material particles limits electron transport in the electrode, increasing grain boundary resistance. Alternatively, we propose here the use of an electrolyte additive to direct in situ the formation of a protective layer, by analogy to the commonly used solid electrolyte interphase (SEI)-forming additives for the graphite negative electrode.

The surface protective layer formed on the positive electrode, typically denoted cathode electrolyte interphase (CEI), has been targeted in previous studies by including, for example, phosphate- or nitrile-based additives,[7–11] although the exact mechanisms of action are in most cases unknown. As such, concrete efforts of CEI-engineering are still on their infancy in comparison to their SEI counterpart. In this study, we propose the use of alkoxy derivatives of $LiAlH_4$ as electrolyte additives to form an Al-based inert layer on the surface of the positive electrode material. Lithium tri(tert-butoxy)hydridoaluminate (LTBA) stands out in this family due to its water-scavenging ability and mild reductive character. The role of LTBA as an electrolyte additive is evaluated on the bare, uncoated Ni-rich layered oxide cathode material ($LiNi_{0.86}Mn_{0.07}Co_{0.07}O_2$, termed NMC86 hereafter) by electrochemical tests, X-ray photoelectron spectroscopy (XPS), and transmission electron microscopy (TEM) analyses. The NMC86 material is selected as a representative example from Ni-rich NMCs as it exhibits a high capacity with typically poor cycling stability.[12] Including LTBA in the electrolyte blend results in a passivation layer coating on the positive electrode, avoiding surface reconstruction and thus extending the cycle life of the cells.

2. Results and Discussion

2.1. Synthesis and Characterization of Lithium Alkoxyaluminates

The methoxy, ethoxy, *iso*-propoxy, and *tert*-butoxy derivatives of $LiAlH_4$ were prepared by a direct reaction of $LiAlH_4$ with the corresponding alcohol. The extent of the hydride to alkoxide substitution around the central Al depends on the nucleophilic character and the steric hindrance of the alcohol.[13,14] Thus, when the three first alcohols are used, the tetra-substituted adduct is obtained: $LiAl(OR)_4$. In the case of the bulky *tert*-butanol, the product corresponds to the tri-substituted adduct: $LiAlH(OR)_3$ (Lithium tri(tert-butoxy)hydridoaluminate – LTBA), which retains an active hydride ligand (inset in **Figure 1a**). Details on the characterization of the first three members of the family are given in the supporting information (Figure S2, Supporting Information), while we will focus here on LTBA, which gives the best performance as electrolyte additive, as will be discussed later.

Chemical analysis of the prepared *in-house* LTBA agrees with the expected composition (Figures S3–S5, Supporting Information). The Li/Al molar ratio obtained by Inductively coupled plasma mass spectrometry (ICP-MS) is close to 1.0, and the liquid ^1H and ^{13}C NMR confirm the presence of the *tert*-butoxy ligands corresponding to the chemical structure of the anion. Finally, we quantified the hydride amount in the material by digesting the product in 10 wt.% HCl and measuring the amount of $H_{2(g)}$ by gas chromatography. A hydride content of 0.39 wt.% in the solid is obtained, corresponding to a stoichiometry of one active hydride per aluminum center.

LTBA is also available commercially from Sigma-Aldrich, although we observed important differences with the *in-house* product, which led us to perform a deep characterization of both materials. Figure 1a displays the infrared (IR) spectra of both solids, highlighting the Al-H stretching band. While the *commercial* LTBA displays a sharp band centered at 1766 cm^{-1}, this band is slightly red-shifted and broadened for the product prepared *in-house*. This is the result of a change in the connectivity of the anion, from a terminal Al – H bond (sharp IR band) to a bridging Al – H···X conformation (broader band).[15] This change in connectivity is also reflected in the appearance of new, relatively broad bending modes at 560 and 843 cm^{-1}. As expected, this change in connectivity also results in different crystal structures for both materials, as evidenced in the powder X-ray diffraction (XRD) pattern (Figure 1b). However, we were not able to solve the structure from powder XRD, and our attempts to obtain single crystals were unsuccessful due to the high sensitivity of the materials to traces of water. Instead, we turned to solid-state NMR to gain more insights into the Al, H, and Li environments.

Figure 1c shows the solid-state ^1H NMR spectra of the two products (in-house in blue and commercial in red), focused on the $-CH_3$ and Al-H regions. In both cases, the presence of the hydride is confirmed by the J-coupling between ^{27}Al and ^1H (^1J = 190–250 Hz) producing a sextuplet centered $\approx\delta$ = 2.5 ppm for *in-house* LTBA and 3.0 ppm for the *commercial* LTBA. The J-coupling is likely combined with a dipolar-quadrupolar cross-term, which gives rise to asymmetric multiplets.[16] The ^{27}Al NMR spectra (Figure 1d) display a broad signal in the range 65–85 ppm, a typical chemical shift range for tetrahedrally coordinated Al complexes, corroborating the structure of the anion.[17] The experimental line shape of the *in-house* LTBA agrees well with the presence of a single Al environment, confirmed by the fitting of the spectrum shown in the inset, where one second-order quadrupolar lineshape for the central transition overlaps with the narrow n = 0 spinning sideband of a satellite transition. In contrast, the line shape of the commercially obtained product displays a more complex splitting, suggesting the presence of at least two different Al environments in the solid, indicating the possibility of some small amount of a secondary/impurity phase in the *commercial* LTBA. The opposite situation appears in the ^7Li NMR spectra. While the *commercial* product shows one single resonance peak centered at −0.3 ppm (with some

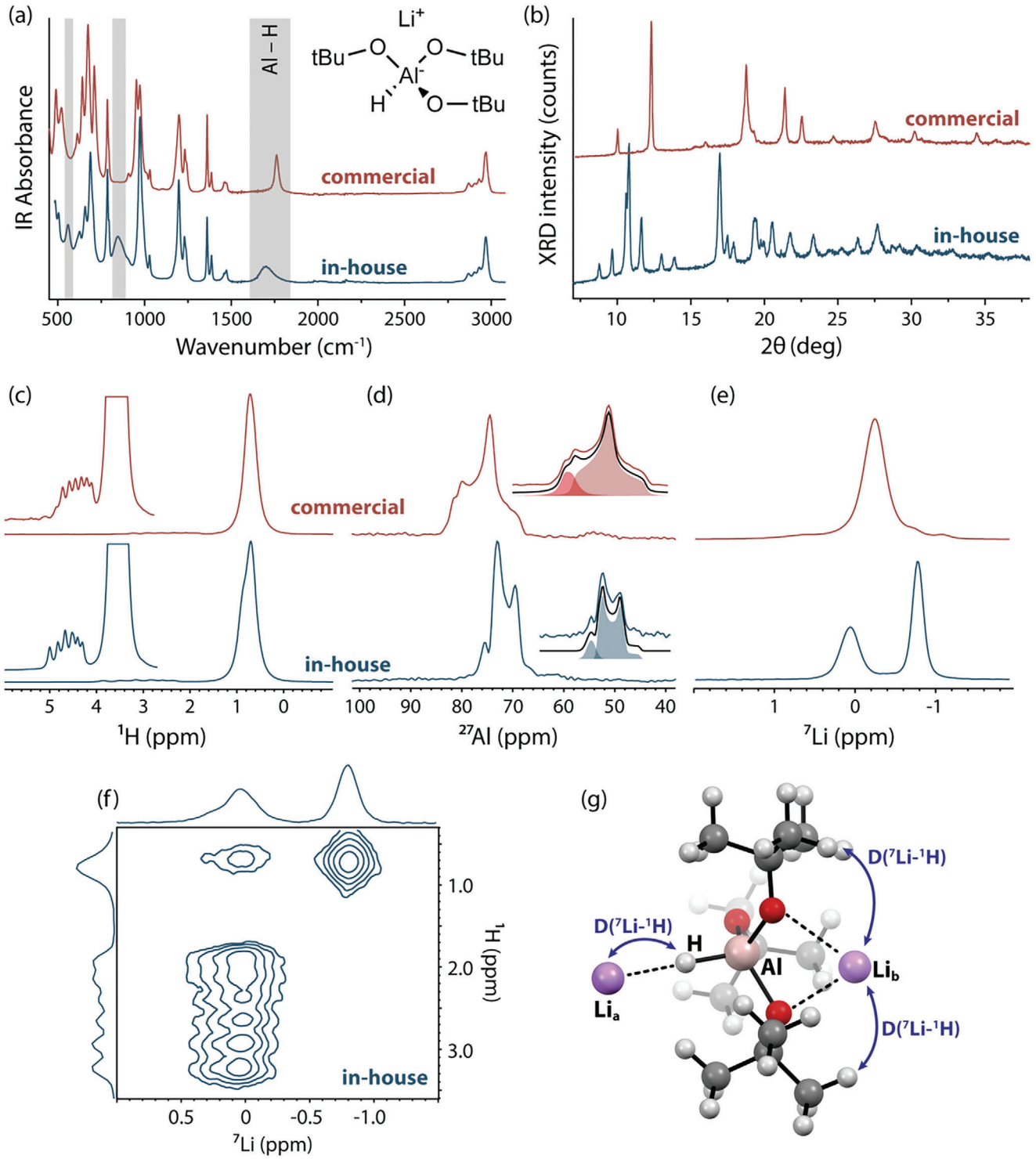

Figure 1. Characterization of LTBA. a) IR spectra of the in-house and commercial LTBA, inset shows the expected chemical structure. b) Powder XRD patterns of the in-house and commercial LTBA. c–e) Solid-state ^{1}H, ^{27}Al, and ^{7}Li NMR spectra respectively. f) $^{1}H \rightarrow {}^{7}Li$ correlation 2D NMR spectra. g) Representation of the LTBA anion structure highlighting the two possible coordination sites for Li^{+} and their respective dipolar coupling D(^{7}Li-^{1}H).

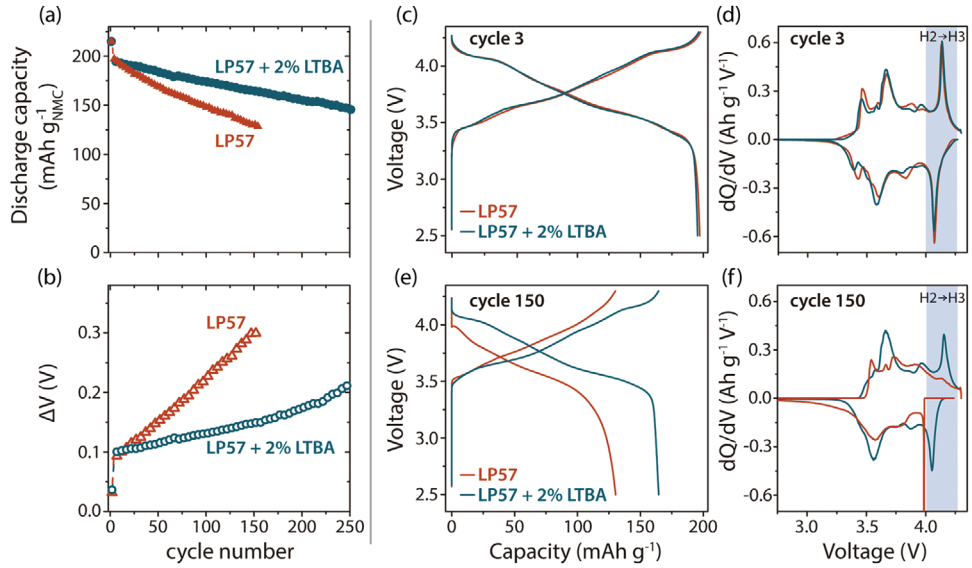

Figure 2. Cycling performance of NMC86 | graphite cells with and without the LTBA additive. a) Capacity retention upon continuous cycling at C/3 constant current (1C = 275 mAh g^{-1}). b) Evolution of the cell polarization ($\Delta V = \tilde{V}_{charge} - \tilde{V}_{discharge}$) upon cycling. The average voltage during charge or discharge is calculated as energy [Wh] divided by capacity [mAh] (only 1 marker every 5 cycles is displayed). c,e) Cycling profiles of the cells at cycle 3 and 150 respectively. d,f) Differential capacity plots of the curves presented in panels (c) and (e) respectively.

impurities around), the product prepared in-house displays two peaks at 0 and −0.8 ppm evidencing two different lithium sites in the crystal (Figure 1e). A ^{1}H-^{7}Li 2D heteronuclear correlation experiment (Figure 1f) allowed us to differentiate the location of the two lithium sites observed in the ^{7}Li spectra of the *in-house* LTBA. While the Li site centered ≈0 ppm is physically close to both H sites (methyl and hydride), the one at -1 ppm interacts only with the methyl protons in the –O*t*Bu sidechains.

Together, these results suggest that the main difference between the two products (except the small amount of secondary impurity in *commercial* LTBA) is the organization of lithium cations around the anion. The *in-house* product crystallizes with two possible lithium sites (denoted Li_a and Li_b sites in Figure 1g), one of which is located near the hydride group, causing a broadening of the Al-H vibration band on the IR. In the case of the commercial product, all lithium atoms are located near the –O*t*Bu sidechains (site Li_b), leaving the hydride as a pendant group and producing a sharper Al-H band.

Despite the differences observed in terms of crystalline structure of both materials, they actually have similar chemical compositions. The Li:Al molar ratio, the active hydride content, and the ^{1}H and ^{13}C liquid NMR of the product correspond well with the *in-house* LTBA, and with the expected values in all cases. Thus, the two materials can be considered allotropes of LTBA, in which the Li^+ positions make the biggest difference. We speculate that the synthesis procedure has a great impact in the formation of one or the other structure, but we lack information about the procedure followed by Sigma-Aldrich to prepare the material. Further studies into these two crystal structures, although intriguing, are beyond the scope of this study, as our aim is to use the material (completely solubilized) as additive in lithium-ion battery electrolytes.

2.2. Use of LTBA as Electrolyte Additive for Li-Ion Batteries

LTBA was found to be insoluble in organic carbonate solvents (ethylene carbonate, propylene carbonate, etc), but was completely solubilised in the presence of a second lithium salt, e.g. $LiPF_6$, irrespective of the anion of the lithium salt used. In the same line, the sodium analog ($NaAlH(OtBu)_3$) is not soluble in solutions containing other sodium cations, and only solubilizes in when an excess Li^+ cations are present (Figure S6, Supporting Information). These observations suggest that the aluminate anion is dissolved as a $[Li\text{-}AlH(OtBu)_3\text{-}Li]^+$ cationic complex, with two different Li^+ coordination sites. This agrees with our view of the different Li^+ positions in the crystal structure discussed in the previous section (Figure 1g).

We prepared 1 M $LiPF_6$ electrolytes in EC:EMC 3:7 volume ratio (known as LP57) with the addition of LTBA in different concentrations, with 2 wt.% displaying the best performance ([LTBA] ≈0.1 M). Following formation (2 cycles at C/10 rate), the cells were cycled in the 2.5-4.3 V versus graphite at a constant C/3 rate (1C = 275 mA/g_{NMC}). The presence of LTBA in the electrolyte significantly increases the capacity retention of the cells and avoided the fast polarisation increase observed in the control electrolyte (**Figure 2**a,b). These beneficial effects were observed for both *commercial* and *in-house* LTBA (Figure S7, Supporting Information). However, the *in-house* product demonstrated better performance, possibly due to its higher purity as determined by solid-state NMR analysis. Consequently, further analyses focused only on *in-house* LTBA.

After 150 cycles, the cell containing the control LP57 electrolyte has lost around 40% of its initial capacity, agreeing with previous reports using uncoated NMC86,[12] while only 25% of the initial capacity is lost while using LTBA additive. The structural degradation of the material, as previously identified as the main reason for such capacity fade, is evidenced here in the

evolution of the voltage profile and dQ/dV plots for the cycles 3 and 150 (Figure 2c-f). In the initial cycles, the cycling profile and the derivative plot correspond with the expected for the NMC86|graphite full cell, including the sharp peak assigned to the H2 → H3 phase transition of the cathode material, ≈4.1 V. After 150 cycles, this high-voltage transition has completely disappeared, while many of the other peaks have decreased in intensity. In contrast, the cells containing the Al additive still display a similar voltage profile retaining the high-voltage transition after 150 cycles, and even after 270 cycles (Figure S8, Supporting Information). Clearly, the presence of the additive results in an increased structural stability of the cathode material, which arises from the combination of two beneficial effects we will explore next.

2.3. Exploring the Action Mechanism of LTBA

Given its mild reducing character, we hypothesize that LTBA increases the cycling life of the NMC86 electrode through two mechanisms: *i)* it consumes water and other protic impurities in the electrolyte, preventing formation of HF and avoiding transition metal dissolution; and *ii)* it interacts with the NMC86 surface, producing an Al-rich CEI and preventing surface reconstruction.

To evaluate the effectiveness of the additive to remove acidic impurities, an aliquot of 1000 ppm of water was added to both the control LP57 electrolyte and the electrolyte containing LTBA. After 24 hours of ageing, the liquid ^{19}F NMR spectrum was recorded for both electrolytes (**Figure 3a**). The presence of water in the control electrolyte caused the hydrolysis of the anion, producing HF (δ -190 ppm) and $PO_2F_2^-$ (δ −85.6 ppm). The electrolyte containing the LTBA additive, on the other hand, showed no signs of anion decomposition and no HF formation, thereby potentially reducing electrode attack by hydrofluoric acid and active material loss. Indeed, we observed a significant decrease in the transition metal dissolved from the NMC86 when LTBA is present in the electrolyte (Figure 3b). Previous reports have highlighted the detrimental effect of dissolved Ni and other transition metal cations in the cycling performance of lithium-ion cells and thus this protection mechanism is expected to contribute to the increased cycle life of the NMC86 | graphite cells observed.[18]

However, the dissolution of the active material is not the only degradation phenomenon that LTBA is avoiding. The second protection mechanism involves the oxidation of the additive on the surface of the NMC particles to form an Al-rich protective layer. The cyclic voltammetry (CV) of the LTBA-containing electrolyte, recorded on a glassy carbon electrode, shows a higher oxidative current on the operating window of the studied cathode (up to 4.3 V versus Li) than the control LP57 electrolyte (Figure 3c). During this oxidation process, the additive decomposes to produce a passivating layer, as suggested by the decrease of the oxidation peak in the subsequent CV cycles (Figure S9, Supporting Information).

To gain further evidence of the formed CEI on the positive electrode material, the NMC86 electrodes were recovered either after formation cycle or after 155 cycles and were analyzed by XPS and TEM (**Figures 4** and 5). When cycled in LP57, the chemical composition of the NMC surface remains almost unaltered, with all the peaks in the C 1s, O 1s, and F 1s XPS spectra being easily identified to the PVDF, Csp, and NMC. Only small contributions from surface deposits of LiF and some deposited carbon species are detected.

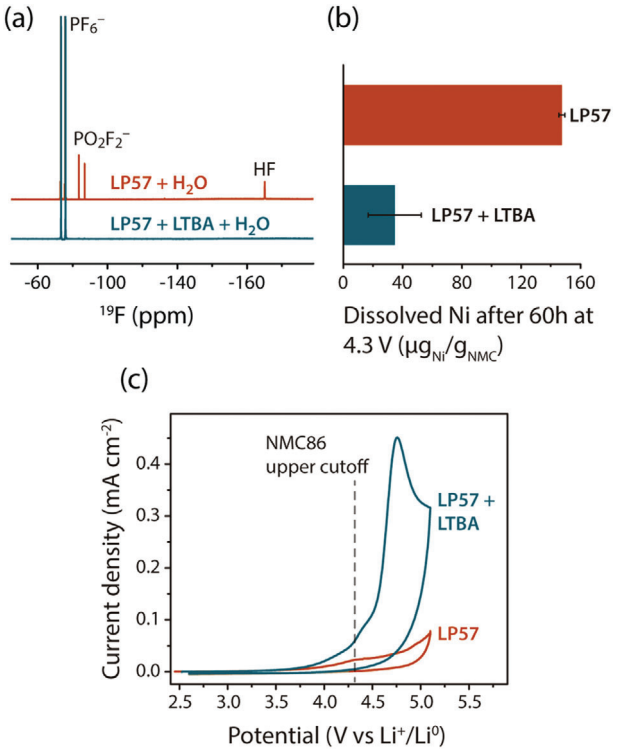

Figure 3. Evidences of the beneficial effects of LTBA additive. a) ^{19}F NMR of the LP57 and LP57 + LTBA electrolytes after addition of 1000 ppm of water and 24 h ageing. b) Amount of nickel dissolved from the active material after holding a full NMC | graphite cell at 4.3 V for 60 h. The error bars represent the standard deviation over two identical cells. c) Cyclic voltammogram of the two electrolytes over glassy carbon electrodes showing the oxidation of the additive (scan at 20 mV s^{-1}).

In contrast, when LTBA is present in the electrolyte formulation, the XPS spectrum displays a sharp, intense peak at 75.5 eV, which is ascribed to Al 2p in oxygenated environment such as Al_2O_3 or similar. The arising of this peak comes with a significant decrease of the NMC peak's intensity in the O 1s spectrum, and of the PVdF and Csp peaks in the C 1s spectra. This suggests that a surface layer is formed on top of the electrode during formation, and it evolves during cycling further burying the signal of the active material and binder after 155 cycles. In the C 1s spectra, an intense contribution is recorded at 286.7 eV (marked in dark blue) attributed to C-O bonds. However, the $-CH_3$ concentration does not correspond to the expected if the –O*t*Bu were taking part of the surface layer, which suggests that the observed C-O moieties are derived probably from some solvent decomposition that takes place during the formation of the CEI.

TEM analyses allowed us to go deeper into the morphology of this Al-based protective coating and its effect on the NMC86 stability. As in the case of XPS, the NMC materials were recovered from cells right after the formation cycle and after 155 cycles, using either the control LP57 electrolyte or the electrolyte

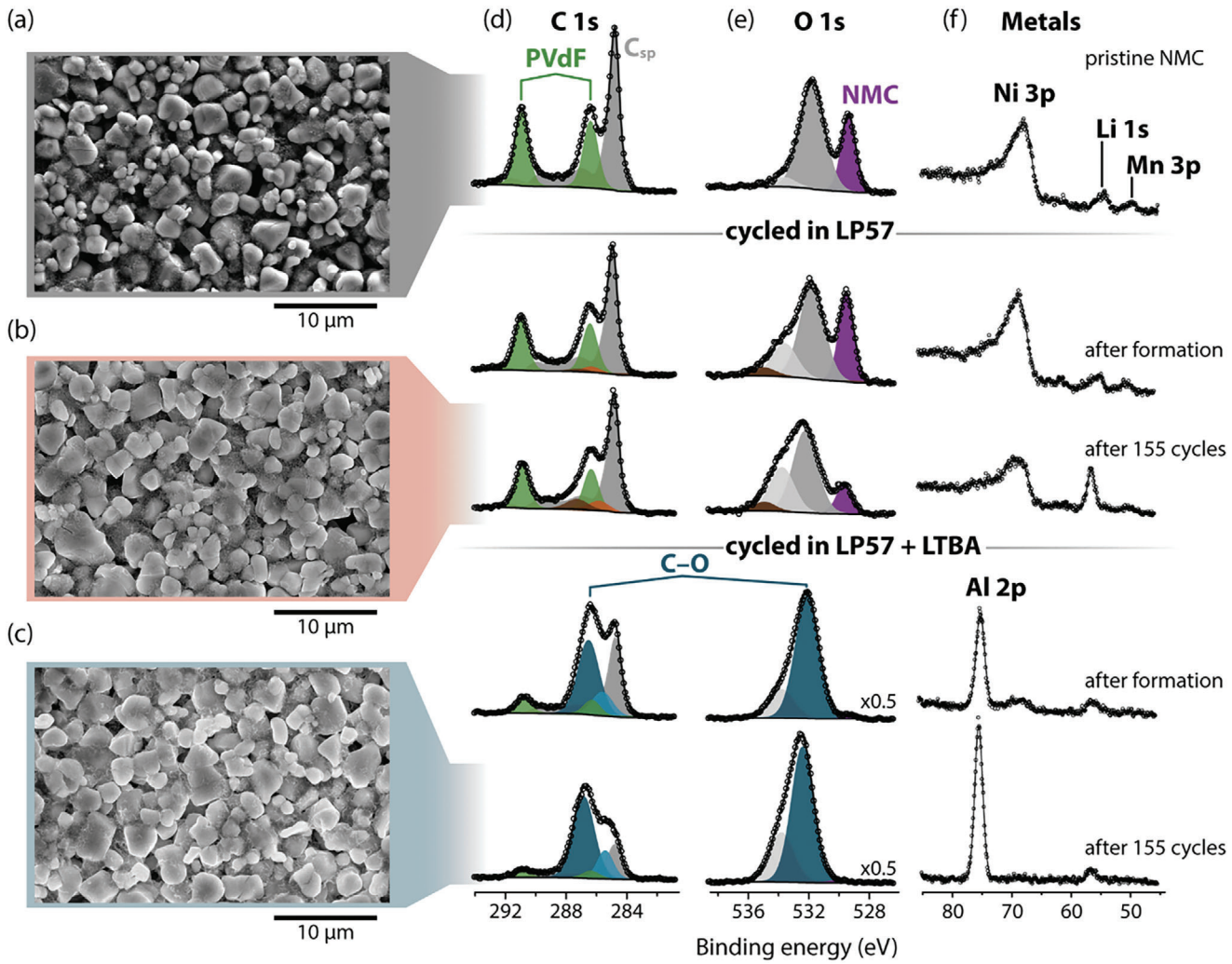

Figure 4. Surface analysis of pristine and cycled NMC86 electrode. a–c) SEM pictures of the pristine electrode, the electrode cycled in LP57 electrolyte, and the electrode cycled in LP57 + 2% LTBA, respectively. d–f) C1s, O1s, and metal cation regions of XPS spectra of the pristine electrode surface, and the electrode right after formation cycles and after 155 cycles for the two electrolyte formulations under study.

with 2 wt.% LTBA added. All the electrodes were recovered in discharged state, washed with DMC, and mounted on TEM grids without air exposure (see experimental description). The LTBA additive decomposes on the surface of NMC86 particles forming an Al-rich layer, evident in the energy-dispersive X-ray spectroscopy (EDX)-STEM elemental maps (Figure 5a-h; Figure S10, Supporting Information). Some isolated Al-rich particles are also observed although it is not clear if they are formed chemically (e.g., by additive hydrolysis), electrochemically (e.g., by additive oxidation), or during sample preparation.

The coating layer around the NMC86 particles has a non-uniform thickness between 50 and 150 nm (Figure 5e) and is composed of C, O, F, and P, with traces of Ni (<1 at. %), which largely accompany the Al distribution (Figure S11, Supporting Information). The carbon content varies significantly from ≈19 at.% to 60 at.%. The O:F:Al:P atomic ratio is also not homogeneous and can roughly be quantified to 41(7):35(6):18(4):6(2).

The local structure of NMC86 after 155 charge/discharge cycles was analyzed by selected area electron diffraction (SAED) and high angle annular dark field scanning transmission electron microscopy (HAADF-STEM). In the SAED patterns, shown in Figure S12 (Supporting Information), the main reflections correspond only to the trigonal *R*-3m lattice with a ≈2.9 Å and c ≈14.2 Å characteristic of the underlying O3-type stacking. The O3-type stacking is also evident in the [100] HAADF-STEM images (Figure 5i,j), as the bright dots corresponding to the transition metal (TM) columns laterally shift by 1/3 of the inter-dot distance. The crystal structure of the NMC cycled with the control electrolyte shows pronounced interlayer Li/TM disorder (Figure 5i, exemplified with the enlarged insert). This cation-disordered rock-salt-type layers spans over ≈10 nm from the surface. Contrarily, in the NMC86 cycled in the LTBA-containing electrolyte (Figure 5j) the disorder is only partial and the thickness is limited to 2–3 nm.

In order to highlight the differences in degradation after 155 charge/discharge cycles of NMC86 with and without the Al additive a spatial distribution of the Ni oxidation state in the samples was mapped by electron energy loss spectroscopy

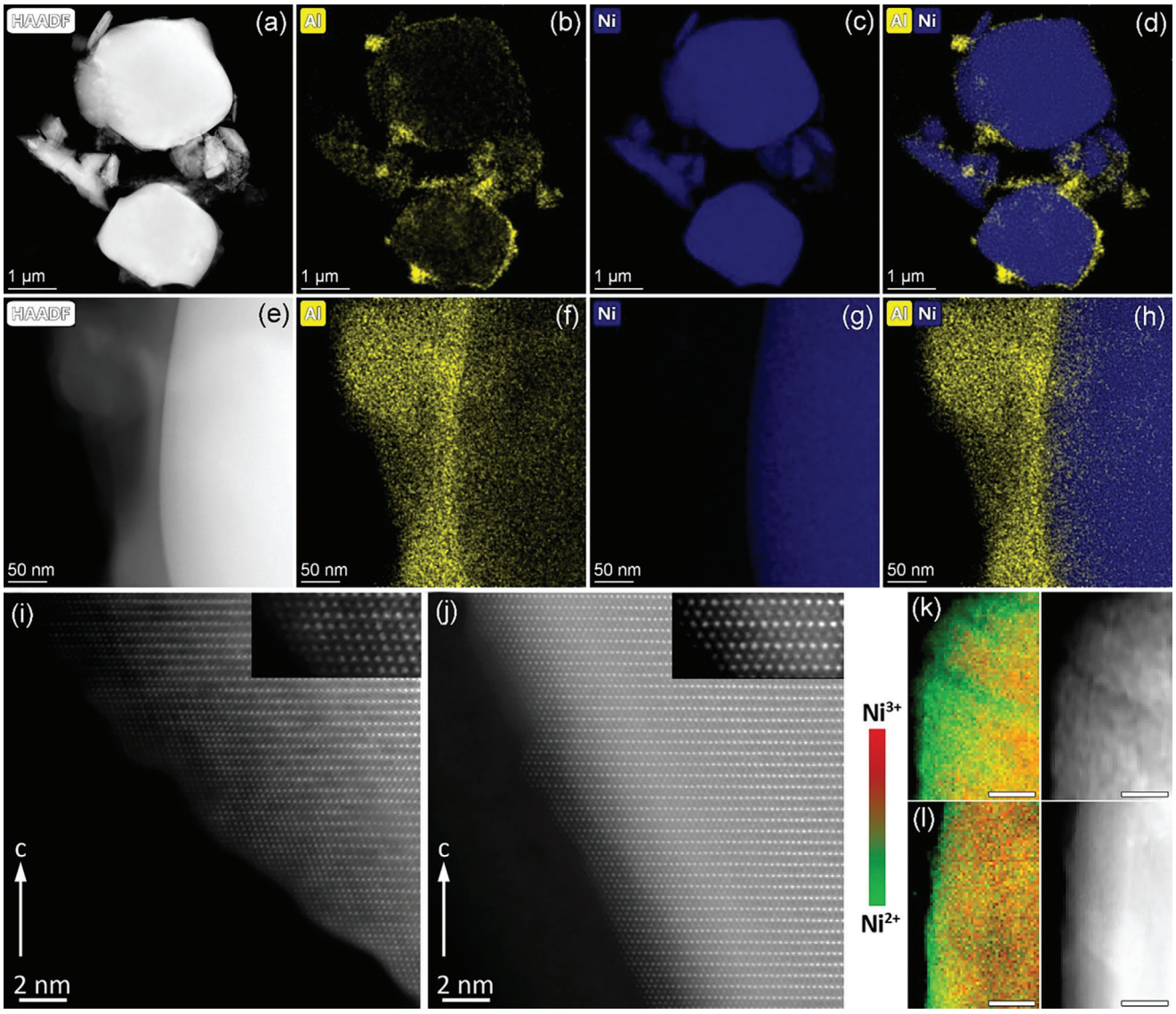

Figure 5. TEM analysis of the NMC86 material after cycling. a,e) HAADF-STEM images of the material after 155 cycles in the LTBA electrolyte. b–d) and f–h) color-coded elemental EDX maps of the areas shown in panels (a) and (e), respectively. (i,j) [100] HAADF-STEM images of the materials after cycling in LP57 electrolyte i) and after cycling in a LTBA containing electrolyte (j) and inserted magnified surface images demonstrating cation disorder. k,l) color-coded STEM-EELS maps of the Ni oxidation state near the surface of the NMC86 particles after cycling in LP57 electrolyte (k) and in a LTBA containing electrolyte (l). The Ni^{2+} and Ni^{3+} contributions are denoted in green and red colors, respectively. The scale bar is 20 nm.

(EELS)-STEM method based on the intensity of the Ni-L_2 edge according to the methodology from Ref. [19] (Figure 5k,l). Obtained color-coded EELS maps demonstrate that for NMC86 cycled in the LTBA electrolyte the reduced Ni species concentrate at the very thin surface layer of 2–5 nm, whereas for the cycled in LP57 electrolyte the reduced layer deepens by 10–20 nm into the bulk. Such behavior nicely corroborates the HAADF-STEM results. Overall, the TEM analyses indicate that the electrode-electrolyte reactivity has been suppressed by Al-based coating using LTBA additive, hence the crystal structure is maintained in O3 with comparatively less changes in the surface from the Ni-reduction, cation mixing, and conversion to cation disordered rock-salt structure, in comparison to the bare NMC86 without Al-coating.

2.4. Role of the Negative Electrode on the Cycling of NMC86 using LTBA Electrolyte Additive

Aside from the beneficial effects of the additive on the stability of the NMC86 cathode material, two observations lead us to consider that LTBA also participates in SEI formation on the graphite negative electrode. First, the cathodic branch of the cyclic voltammogram shows that the presence of the aluminium additive modifies substantially the characteristic EC reduction waves observed in the control LP57 electrolyte (Figure S13, Supporting Information). Second, the XPS spectra of the recovered graphite evidence the presence of aluminum products on the surface, similar to the ones observed on the NMC86 surface (Figure S14, Supporting Information). Therefore, the increased capacity retention for the

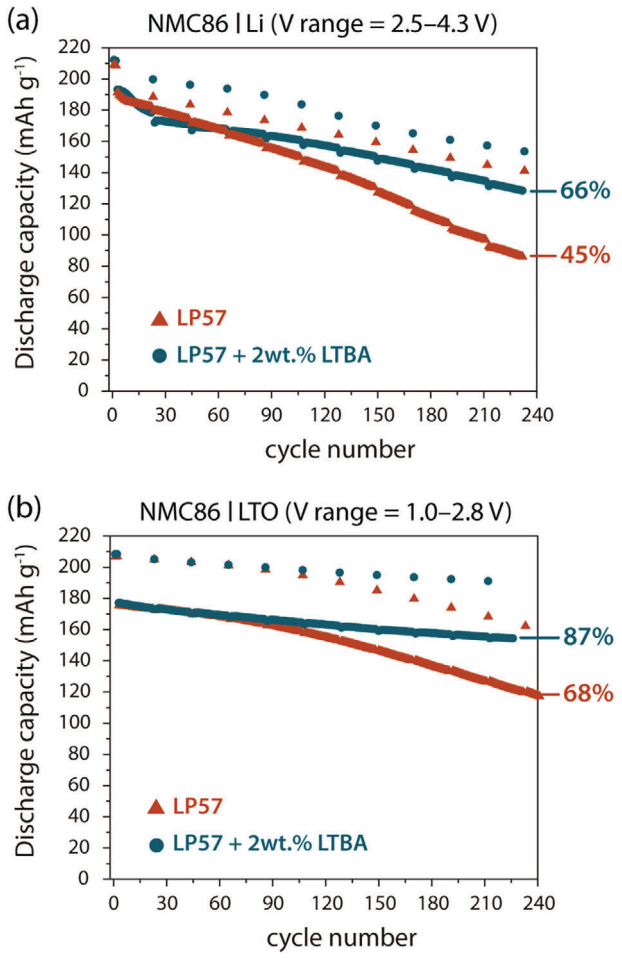

Figure 6. Cycling performance of the NMC86 cells with different counter electrodes. Capacity retention plots for the a, NMC86 | Li a), NMC86 | LTO b) cells using LP57 electrolyte with (blue rounds) and without (maroon triangles) LTBA additive.

full NMC86 | graphite cells could be ascribed to an enhanced stability in either electrode.

To focus more specifically on the positive electrode, and better understand the degradation phenomena, we assembled NMC86 cells with either lithium metal or $Li_4Ti_5O_{12}$ (LTO) as negative electrode. **Figure 6** shows the capacity retention during cycling at C/3, with one slow cycle at C/20 every 20 cycles for both cell configurations. Assembling cells with lithium metal overcomes degradation processes coming from lithium inventory loss or negative electrode material loss. Nevertheless, the cells containing the control electrolyte display still a significant capacity fading of ≈0.3% per cycle and ≈60% loss in 200 cycles (Figure 6a). The NMC86 material degrades faster than the most commonly studied NMC811 which highlights the challenges of moving toward increasingly higher Ni-content cathode materials, as other authors have previously acknowledged.[12,20]

Additionally, in the NMC86 | Li cell, the capacity recovered at low rates (C/20) and at high rates (C/3) continuously diverge. Together with the capacity fading, these phenomena suggest some degree of surface reconstruction of the NMC86 material, as observed before in the HAADF-STEM images, which causes a continuous increase in the impedance of the cell by blocking the Li diffusion pathways. By adding 2 wt.% of LTBA, the presence of the protective layer on the active material particles prevents the uncontrolled impedance buildup and thus extends the cycling life.

However, the low operating potential of Li metal will still promote electrolyte decomposition, and possibly the formation of soluble products, which can lead to cross talking between positive and negative electrodes. Such degradation effects are avoided by employing an oversized LTO as counter electrode. Better capacity retention is observed with NMC86|LTO cells, where 87% of capacity is retained after 240 cycles when LTBA is used (Figure 6b). The extended cycling life obtained when moving from graphite to LTO suggests the graphite electrode degradation is contributing significantly to the capacity fading observed in NMC86|graphite cells, possibly due to an unstable SEI layer.

Further electrolyte optimization can be done by combining LTBA with other previously reported additives. Particularly, the use of $LiPO_2F_2$ has been previously studied in NMC-based lithium-ion batteries with different Ni compositions,[21,22] and its beneficial role on the formation of the SEI on the graphite electrode has been demonstrated.[23] In this study, we observed that the combination of 2 wt.% LTBA + 1 wt.% $LiPO_2F_2$ can further increase the cycle life of NMC86|graphite cells, displaying less than 10% capacity fade after 200 cycles (Figure S15, Supporting Information). The exact mechanisms of action of this additive blend is intriguing, and will be a subject of study of future reports.

3. Conclusion

In this study, we provide novel insights into the coordination behavior of the tri(*tert*-butoxy)hydridoaluminate anion toward lithium cations, both in solid and in solution. Although the determination of the crystal structure remains elusive, our results suggest that two Li coordination sites exist around the aluminate anion: one close to the hydride ligand and one close to the –O*t*Bu side chains, resulting in two different allotropes observed here. The population of these two coordination modulates the solubility of the compound in polar organic solvents, such as carbonates, and thus in its use as an electrolyte additive for lithium-ion batteries.

We have shown that the use of this compound as an electrolyte additive extends the cycle life of Ni-rich based cells, when using either graphite, LTO, or Li metal as counter electrodes. The success of this additive results from its capacity to scavenge acidic impurities, and to form a protective surface layer over the cathode material particles. The Al-based protective coating, formed electrochemically in situ, prevents material degradation, avoids oxygen abstraction from the material, and reduce transition metal migration. This study represents the first example of a hydridoaluminate used as electrolyte additive for lithium-ion batteries, and opens the door to explore other related compounds in order to optimize the CEI composition and performance.

Furthermore, this strategy of in situ generated coatings opens the possibility to design new CEI-forming additives that could mimic other coatings such as $LiNbO_3$, typically found to be very efficient in reducing the surface reactivity. This would unlock the long cycling stability of other high-voltage cathode materials, such as Li-rich layered oxides or $LiNi_{0.5}Mn_{1.5}O_4$ spinel. We

believe that the CEI-engineering strategy pursued in this study will be crucial in the development of future advanced and more powerful, lithium-ion batteries.

4. Experimental Section

Synthesis and Characterization of Materials: The preparation and purification of the aluminates was performed in an Ar-filled glovebox (O_2 <1.0 ppm; H_2O <0.1 ppm). A solution of ≈0.1 M $LiAlH_4$ in diethyl ether was prepared by dilution from a commercial 4.0 M solution (ThermoFisher Scientific) using dry diethyl ether. The corresponding alcohol (MeOH, EtOH, *i*-PrOH, or *t*-BuOH) was added dropwise to the lithium alanate solution at room temperature, with evident formation of H_2 gas. A 0.2 eq. excess of the alcohol was used to guarantee the complete reaction of the alanate. After 1 h of stirring, the formed solid was recovered by centrifugation, washed several times with fresh diethyl ether, and dried under vacuum. Sodium tri(tert-butoxy)hydridoaluminate (NTBA) was prepared following a similar procedure but starting from solid $NaAlH_4$ and using dry tetrahydrofuran as solvent.

The obtained products were characterized by Fourier-transformed infrared (FTIR) spectroscopy, liquid- and solid-state nuclear magnetic resonance (NMR) spectroscopy, and powder X-ray diffraction (XRD). FTIR spectra were acquired in ATR mode using a diamond crystal on a NicoletTM iSTM 5 spectrometer (Thermo Fisher Scientific) in the range of 400 to 4000 cm^{-1}. XRD patterns were acquired on a Bruker D8 Advance diffractometer with Bragg–Brentano geometry, a Cu-K_α source (λ_1 = 1.54056 Å, λ_2 = 1.54439 Å) and a LynxEye detector. An airtight reflection-based Leriche cell[24] with a Be window was used to enclose samples inside the glovebox.

Liquid NMR spectra were recorded in a Bruker 7.046 T (300 MHz) Advance III NMR spectrometer mounted with a 5 mm HX(F) probehead. THF-d8 (99.5% D, Eurisotop) was used as solvent, previously dried over activated molecular sieves. The residual solvents peaks were used as reference for ^1H and ^{13}C, while the reported chemical shift of PF_6^- was used as reference for ^{19}F (ref. [25]).

Solid-state NMR spectra were recorded on a Bruker 20 T (850 MHz for ^1H) wide bore spectrometer equipped with an Advance NEO console, and a triple resonance $^1H/X/Y$ Magic Angle Spinning probe with a 1.3 mm rotor diameter. 1.3 mm rotors were filled with the samples in argon filled glove box and the MAS bearing and drive gas was N_2 to avoid unwanted reactions, and the rotors were spinning at 62.5 kHz. The chemical shifts were referenced against TMS at 0 ppm for ^1H, 1 M LiCl in water for ^7Li and 1 M $Al(NO_3)_3$ in water for ^{27}Al.

^1H NMR Spectra: The ^1H NMR spectra were recorded using a Hahn echo sequence synchronized with the rotation, with an echo half-time of one rotor period (16 µs). The RF field was set to 118 kHz, with a 90° pulse of 2.125 µs. The magnetization recovery delay was set to 15s, which was largely sufficient to ensure the recovery of the whole magnetization, as the longitudinal relaxation times of the hydride hydrogen were measured at 2.8 s (*in-house* LTBA) and 1.3 s (*commercial* LTBA), 1.1 s and 0.58 s for the methyl groups hydrogen atoms (*in-house* and *commercial*, respectively). Integration of the signals lead to a ratio of the NMR peak areas methyl/hydride of 21 in the commercial sample, and 23 for the house made LTBA. The expected ratio is normally 27, and therefore, it is likely as there is an excess of signal in the hydride region, which may come from impurities with resonance overlapping with the hydride sextuplets, or from methyl magnetization loss during the echo time. This discrepancy is not observed in the liquid phase NMR spectra.

^{27}Al NMR Spectra: The ^{27}Al NMR spectra were recorded using a single, short 0.46 µs pulse excitation ($\pi/18$ for quantitative measurements for quadrupolar spin 5/2 nuclei) at 60 kHz nutation frequency followed by ^1H decoupling, using a PISSARRO decoupling sequence[26] with a 4.25 µs decoupling pulse at 118 kHz. The recovery delay was set to 1 s, while the longitudinal relaxation times T_1 were measured at 900 ms (*in-house* product) and 600 ms and 10 s for the *commercial* product, which confirms the presence of distinct environments).

^7Li NMR Spectra: The ^7Li NMR spectra were recorded with a single pulse excitation (4.8 µs 90° pulse with an RF field strength of 52 kHz), and a relaxation delay of 200 s was used, as the T_1 values were measured at 40 s for the *house* made LTBA and 14 s for the *commercial* LTBA.

^1H-^7Li HETCOR: The 2D HETeronuclear CORrelation experiment was recorded with a Cross-Polarization transfer of the ^1H magnetization to the ^7Li spins. The contact time was optimized at 160 µs, a constant spin-lock power was applied on the lithium channel, with a 15 kHz RF power, while a 70% to 100% ramp was applied on ^1H, with a maximum power of 88 kHz, which corresponds to the fulfillment of $\omega_H - \omega_{Li} = \omega_r$ halfway through the spin-lock ramp. The sweep width in the indirect dimension was set to 12 500 Hz (i.e., a time increment of 80 µs = 5 τ_r) and 128 points were recorded using the States method for quadrature detection.[27]

The Li:Al and Na:Al ratio in the obtained aluminates was estimated by Inductively Coupled Plasma Mass Spectrometry (ICP-MS, Nexion 2000, Perkin Elmer), following an standard addition protocol. A known amount of the dried solid (~20 mg) was completely dissolved in 2 wt.% aqueous solution of HNO_3. Five different samples, with five different concentrations of added Li, Na, and Al standard, were measured by ICP-MS, and the concentration of the unknown sample was determined by linear extrapolation (see details in Figure S3, Supporting Information).[28]

Quantitative gas chromatography (GC) analysis was employed to assess the hydride content of LTBA and NTBA (Supplementary Figure S5, Supporting Information). A known amount (≈15 mg) of the material was weighted in a round-bottom flask and closed with a septum inside an Ar-filled glovebox. The flask was removed from the glovebox and 0.4 mL of 10 wt.% HCl solution in water was injected, with evident bubbling and complete dissolution of the solid. An aliquot of the headspace gas was collected and injected on the GC system. Gas chromatography was performed with a Multi-Gas Analyzer #5, equipped with a Thermal Conductivity Detector (TCD) and MoleSieve 5A columns, maintained at a column temperature of 50 °C and an argon carrier gas at 50 psi. The calibration curve for the method was obtained by reacting known amounts of sodium metal with HCl, following the same procedure used to digest the LTBA samples.

The electrochemical stability window of the electrolyte, and the role of the Al-based additive were assessed by cyclic voltammetry in a classical three-electrode cell, following previous reports from our group.[29] A non-aqueous Ag/Ag^+ electrode was used as reference, calibrated against Li metal. Glassy carbon and Pt mesh were used as working and counter electrodes respectively. A cyclic rate of 20 mV s^{-1} was used in all measurements.

Coin Cell Assembly, Testing, and Post-Mortem Analysis: The NMC electrodes were prepared from Ni-rich layered oxide material received from Umicore the composition of which was found to be $LiNi_{0.86}Mn_{0.07}Co_{0.07}O_2$ (denoted NMC86) by ICP-MS and EDX-TEM. The slurry was made by mixing NMC86 powder with C65 carbon black, and polyvinylidene difluoride (PVDF) in a 95:3:2 ratio and using N-methyl-2-pyrrolidone (NMP) as solvent. The slurry was casted on aluminum foil using a doctor blade, and let dry at 80 °C. The coated electrode was cut into disks of 14 mm diameter before a final drying step at 80 °C under vacuum overnight. The obtained active material loading was ≈5 mg cm^{-2}. Graphite electrodes were prepared similarly but using styrene butadiene rubber (SBR) and carboxymethylcellulose (CMC) as binders, to obtain a final composition of 94:2:2:2 and an active material loading ≈3.5 mg cm^{-2}.

2032-type coin cells were assembled inside an Ar-filled glovebox using the previously dried electrodes and two glass fiber disks as separator. As counter electrode, either graphite, lithium metal, or $Li_4Ti_5O_{12}$ (LTO; powder mixed with 5% Csp) were employed. In the case of NMC86 | LTO cells, an excess of LTO counter electrode was used to guarantee enough capacity to achieve full discharge of the NMC (1.6 g_{LTO}/g_{NMC}). The control electrolyte was a 1 M solution of $LiPF_6$ in ethylene carbonate: ethyl methyl carbonate (EC:EMC 3:7 weight ratio), commonly known as LP57. The solvent blend was dried over activated molecular sieves for several days before preparing the electrolyte.

After cycling, the cells were opened in an Ar-filled glovebox and the electrodes recovered, washed with DMC, and dried under vacuum for further analysis. Scanning electron microscopy (SEM) was used to obtain top views of the electrodes before and after cycling and evaluate their morphologies. SEM pictures were acquired using a FEI Magellan

microscope equipped with an Oxford Instruments energy-dispersive X-ray spectroscopy (EDX) detector. The surface chemical composition was studied by X-ray photoelectron spectroscopy (XPS) using a THERMO Escalab 250Xi spectrometer, using focused monochromatic Al K_α radiation ($h\nu$ = 1486.6 eV). The samples were never in contact with air or moisture from their preparation to their analysis since the XPS spectrometer is directly connected to an argon-filled glove box. Peaks were recorded with constant pass energy of 20 eV. The analyzed area of the samples was an ellipse with a dimension of 650 µm × 400 µm. The charge neutralization was used for all the acquisitions. The pressure in the analysis chamber was $\approx 2\times10^{-7}$ mbar during analyses. Short acquisition time spectra were recorded before each experiment to check that the samples were not subject to degradation during the X-ray irradiation. The binding energy scale was calibrated using the C 1s peak at 290.9 eV characteristic of the CF_2 of the PVdF binder. The curves fit for core peaks were obtained using a minimum number of components.

Additionally, the NMC86 materials were scratched from the current collector after cycling and analyzed by transmission electron microscopy (TEM). The samples were prepared in an Ar-filled glovebox by crushing the crystals with an agate mortar and pestle under dimethyl carbonate (DMC) and depositing a drop of suspension onto a carbon film supported by a copper grid. Vacuum transfer holder was used to transfer the samples from the glovebox to microscope column without contact with air. High angle annular dark field scanning transmission electron microscopy (HAADF-STEM) images, selected area electron diffraction (SAED) patterns, energy dispersive X-ray spectroscopy (EDX) and electron energy-loss spectroscopy (EELS) maps were acquired on a probe aberration-corrected Titan Themis Z transmission electron microscope at 200 kV equipped with a Super-X system for EDX analysis and a Gatan Quantum 965 spectrometer for the EELS measurements.

The transition-metal dissolution from the NMC86 material was measured in full cells (NMC | graphite). The cells were assembled as described before and were charged at C/20 rate up to 4.3 V followed by a potentiostatic hold for 60 hours. The cells were immediately disassembled, and the graphite electrode was collected together with one of the two glass fiber separators (the one directly in contact with the graphite electrode). The electrode and separator were digested in 5 wt.% HNO_3 overnight, then filtered and diluted to obtain samples suitable for ICP-MS. The chemical composition was measured in the ICP-MS machine described above. As we recover only one of the two separators in the cell, the quantification of the transition metal dissolved is always underestimated. However, comparison between different electrolyte formulations is still feasible, and its validity was confirmed by reproducing the experiment at least twice, obtaining similar results.

Supporting Information

Supporting Information is available from the Wiley Online Library or from the author.

Acknowledgements

The authors are greatly thankful to Dr. Raphaël Janot (Laboratoire de Réactivité et Chimie des Solides, LRCS) for providing the $NaAlH_4$ used in this study. Regarding financial support, the authors acknowledge the IR INFRANALYTICS FR2054 for access to the 850 MHz solid-state NMR spectrometer and the RS2E Network for funding (French National Research Agency STORE-EX Labex Project ANR-10-LABX-76–01). I.A.M. and A.M.A. are grateful to the Russian Science Foundation for financial support (grant 23-73-30003).

Conflict of Interest

The Centre National de la Recherche Scientifique (CNRS), Collège de France, and Sorbonne Université have filed a patent application (EP23315368.3) based on this work, pending approval. J.F.S, S.M., and J.M.T are named as inventors on this patent application. The other authors declare no conflict of interest.

Data Availability Statement

The data that support the findings of this study are available from the corresponding author upon reasonable request.

Keywords

acid scavenger, Al-based surface coating, cycle life, electrolyte additive, Ni-rich layered oxides

Received: May 10, 2024
Revised: May 30, 2024
Published online:

[1] S. Lee, L. Su, A. Mesnier, Z. Cui, A. Manthiram, *Joule* **2023**, *7*, 2430.
[2] A. O. Kondrakov, A. Schmidt, J. Xu, H. Geßwein, R. Mönig, P. Hartmann, H. Sommer, T. Brezesinski, J. Janek, *J. Phys. Chem. C* **2017**, *121*, 3286.
[3] L. Ni, S. Zhang, A. Di, W. Deng, G. Zou, H. Hou, X. Ji, *Adv. Energy Mater.* **2022**, *12*, 2201510.
[4] F. Lin, I. M. Markus, D. Nordlund, T.-C. Weng, M. D. Asta, H. L. Xin, M. M. Doeff, *Nat. Commun.* **2014**, *5*, 3529.
[5] C. Xu, K. Märker, J. Lee, A. Mahadevegowda, P. J. Reeves, S. J. Day, M. F. Groh, S. P. Emge, C. Ducati, B. Layla Mehdi, C. C. Tang, C. P. Grey, *Nat. Mater.* **2021**, *20*, 84.
[6] G. Kaur, B. D. Gates, *J. Electrochem. Soc.* **2022**, *169*, 043504.
[7] J. Zhang, J. Wang, J. Yang, Y. NuLi, *Electrochim. Acta* **2014**, *117*, 99.
[8] K. Beltrop, S. Klein, R. Nölle, A. Wilken, J. J. Lee, T. K.-J. Köster, J. Reiter, L. Tao, C. Liang, M. Winter, X. Qi, T. Placke, *Chem. Mater.* **2018**, *30*, 2726.
[9] G.-Y. Kim, J. R. Dahn, *J. Electrochem. Soc.* **2015**, *162*, A437.
[10] W. Wang, H. Hu, X. Zeng, Z. Ma, W. Fan, C. Fan, X. Zuo, J. Nan, *J. Power Sources* **2022**, *542*, 231799.
[11] B. A. Sadeghi, C. Wölke, F. Pfeiffer, M. Baghernejad, M. Winter, *J. Power Sources* **2023**, *557*, 232570.
[12] H.-J. Noh, S. Youn, C. S. Yoon, Y.-K. Sun, *J. Power Sources* **2013**, *233*, 121.
[13] H. C. Brown, R. F. McFarlin, *J. Am. Chem. Soc.* **1958**, *80*, 5372.
[14] H. C. Brown, C. J. Shoaf, *J. Am. Chem. Soc.* **1964**, *86*, 1079.
[15] H. Nöth, A. Schlegel, J. Knizek, I. Krossing, W. Ponikwar, T. Seifert, *Chem. – Eur. J.* **1998**, *4*, 2191.
[16] M. Deschamps, D. Massiot, In *Encyclopedia of Magnetic Resonance*, (Ed.: R. K. Harris), John Wiley & Sons, Ltd, Chichester, UK, **2011**.
[17] M. Haouas, F. Taulelle, C. Martineau, *Prog. Nucl. Magn. Reson. Spectrosc.* **2016**, *94–95*, 11.
[18] V. Meunier, M. L. De Souza, M. Morcrette, A. Grimaud, *J. Electrochem. Soc.* **2022**, *169*, 070506.
[19] A. V. Morozov, I. A. Moiseev, A. A. Savina, A. O. Boev, D. A. Aksyonov, L. Zhang, P. A. Morozova, V. A. Nikitina, E. M. Pazhetnov, E. J. Berg, S. S. Fedotov, J.-M. Tarascon, E. V. Antipov, A. M. Abakumov, *Chem. Mater.* **2022**, *34*, 6779.
[20] A. A. Savina, A. M. Abakumov, *Benchmarking the Electrochemical Parameters of the LiNi0.8Mn0.1Co0.1O2 Positive Electrode Material for Li-Ion Batteries*, Heliyon, , **2023**, *9*, e21881.

[21] S. Tan, Z. Shadike, J. Li, X. Wang, Y. Yang, R. Lin, A. Cresce, J. Hu, A. Hunt, I. Waluyo, L. Ma, F. Monaco, P. Cloetens, J. Xiao, Y. Liu, X.-Q. Yang, K. Xu, E. Hu, *Nat. Energy* **2022**, *7*, 484.
[22] D. S. Hall, T. Hynes, C. P. Aiken, J. R. Dahn, *J. Electrochem. Soc.* **2020**, *167*, 100538.
[23] K.-E. Kim, J. Y. Jang, I. Park, M.-H. Woo, M.-H. Jeong, W. C. Shin, M. Ue, N.-S. Choi, *Electrochem. Commun.* **2015**, *61*, 121.
[24] J. B. Leriche, S. Hamelet, J. Shu, M. Morcrette, C. Masquelier, G. Ouvrard, M. Zerrouki, P. Soudan, S. Belin, E. Elkaïm, F. Baudelet, *J. Electrochem. Soc.* **2010**, *157*, A606.
[25] J. P. Allen, C. P. Grey, *J. Phys. Chem. C* **2023**, *127*, 4425.
[26] M. Weingarth, G. Bodenhausen, P. Tekely, *J. Magn. Reson.* **2009**, *199*, 238.
[27] M. W. Maciejewski, M. Mobli, A. D. Schuyler, A. S. Stern, J. C. Hoch, in *Novel Sampling Approaches in Higher Dimensional NMR*, (Eds.: M. Billeter, V. Orekhov), Topics in Current Chemistry, Springer Berlin Heidelberg, Berlin, Heidelberg, **2011**, Vol. *316*, pp. 49–77.
[28] D. C. Harris, C. A. Lucy, *Quantitative Chemical Analysis*, Ed 9, Freeman, New York, NY, **2016**.
[29] C. Cometto, G. Yan, S. Mariyappan, J.-M. Tarascon, *J. Electrochem. Soc.* **2019**, *166*, A3723.